


Fracture Wake Patterns in Brittle Solids

Didier Landru^{1,*}, Damien Massy,¹ Nadia Ben Mohamed,¹ Oleg Kononchuk,¹ Frédéric Mazen,² Samuel Tardif,³ and François Rieutord³

¹*SOITEC, Parc Technologique des Fontaines, 38190 Bernin, France*

²*University of Grenoble Alpes, CEA, LETI, MINATEC Campus, 38054 Grenoble, France*

³*University of Grenoble Alpes, CEA, IRIG, MEM, 38000 Grenoble, France*

 (Received 27 August 2020; revised 12 January 2021; accepted 4 February 2021; published 26 February 2021)

The interactions of a moving crack with self-emitted acoustic waves are studied in ion-implanted circular plates of crystalline silicon, where complex reproducible surface patterns made of local roughness variations are observed. A simple geometrical model, considering the sole propagation of A_0 Lamb waves inside the assembly, allows full prediction of all of these pattern shapes and their dependence on system parameters (crack velocity, elastic properties). Acoustic waves propagating along and behind the crack front are shown to play a central role in fracture-pattern formation. When the crack front is curved, surface patterns originate independently of any edge reflection or frequency preselection from acoustic waves propagating along and behind the crack. As in case of Kelvin wake patterns, fracture patterns emerge from geometrically induced coherence.

DOI: [10.1103/PhysRevApplied.15.024068](https://doi.org/10.1103/PhysRevApplied.15.024068)

I. INTRODUCTION

The fracture of brittle materials has been extensively studied to understand structural failures. Interactions of a propagating crack with elastic waves provides key information about crack dynamics through the marks left on the postfracture surfaces. Acoustic waves can be intentionally introduced into the system to study the fracture dynamics [1–4] or be a consequence of loading, plastic deformation, or crack propagation [5,6] like for Wallner lines [7–10]. They can affect the dynamic of cracks through deflections, oscillations, branching, or local velocity changes [11–14]. Even in a stable propagation regime, stress waves are the means by which the crack-front exchanges energy, which limits the crack-velocity increase in finite-thickness sample geometries [15,16]. In most studies, interacting signals propagate in front of or along the crack, like for recently reported “crack-front waves” [17–21]. The crack front is a source of elastic waves, since part of the loading energy is dissipated in the form of acoustic emission [22], spreads throughout the material, and reaches surfaces where it can be detected using piezoelectric sensors [23–25]. Such signals can be very complex due to the multiple trajectories the waves travel in solid structures with effects of dispersion and sample boundaries [26,27].

Fracture is often perceived as an accidental phenomenon that is to be avoided. However, it can also be harnessed in fabrication processes. The implantation of a high dose of

light ions in a crystalline silicon substrate creates a highly damaged layer a few tenths of a micron below the surface. If this substrate is bonded face to face to another wafer, the plane of defects is then buried near the middle of a 1.5-mm-thick silicon plate [28]. Under annealing, the implanted species evolve into a thin layer of pressurized microcracks, covering a significant fraction of the total surface (Fig. 1) [29]. The gas pressure in microcracks can reach several hundreds of MPa, storing enough mechanical energy to allow the rupture of material between cavities. Then, without any external loading, a crack front may spontaneously propagate inside the damaged layer across the entire structure. Because separation occurs in the implanted plane and not at the bonding interface, a large area of the submicron-thin crystalline silicon layer is transferred from one wafer to the other [30,31]. This so-called Smart-CutTM process is industrially used to fabricate silicon-on-insulator (SOI) substrates for microelectronics applications.

This system is an excellent test vehicle for fracture studies and especially to investigate the interaction between a crack front and its acoustic emission. In highly ordered materials, like crystalline silicon, cracks preferentially move along low-energy cleavage planes. Here, the fracture is confined in a few-nanometer-thick plane defined by the population of microcracks. The implanted gas ensures a constant load at the crack position, avoiding relaxations associated with remote boundary loading, making the crack-front propagate into a damaged material that has lost most of its mechanical strength, including anisotropy [32]. The fracture happens over distances of tens of centimeters

*didier.landru@soitec.com

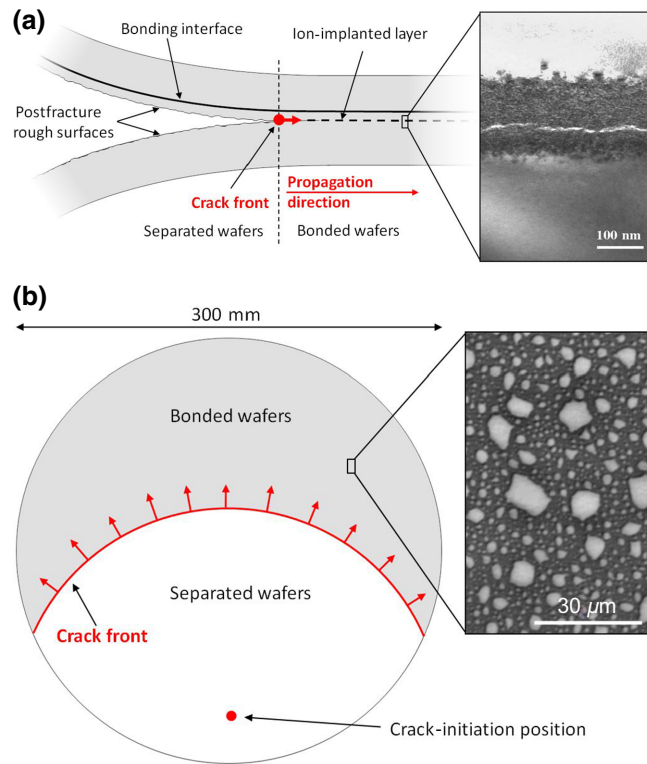


FIG. 1. Schematic of crack propagation in thin silicon-bonded wafers. (a) Side view with a TEM view of microcracks in the ion-implanted wafer. (b) Top view with an infrared microscope transmission of a population of pressurized microcracks in the ion-implanted wafer.

with a remarkably stable crack velocity of several km/s that can be controlled by temperature (i.e., the pressure inside the microcracks) in the moment of the fracture [33]. A crack front with a constant curvature radius is obtained when fracture initiation occurs from a single localized point because its local velocity depends only on temperature and microcrack population, which are constant across the substrate [29]. The assumption that the crack front keeps a smooth circular arc shape centered on its initiation point is confirmed through different experiments (Fig. 2). All direct velocity measurements always give consistent values once the asymptotic crack velocity is reached.

A recent study using ion-implanted silicon highlighted the interaction of a crack front with its own acoustic emission [34]. It demonstrated, in one-dimensional (1D) bar geometry, the possibility to sample the forward-emitted and back-reflected waves. The fracture occurs in a thin plate, thus a part of the crack acoustic emission is converted into Lamb waves [35]. While Lamb waves are extensively used for nondestructive testing of damage in solids [36], their production by a moving crack is less reported [37]. Here, zero-order symmetrical, S_0 , and asymmetrical, A_0 , Lamb modes are detected ahead of the crack front using piezoelectric sensors [34]. The crack front is

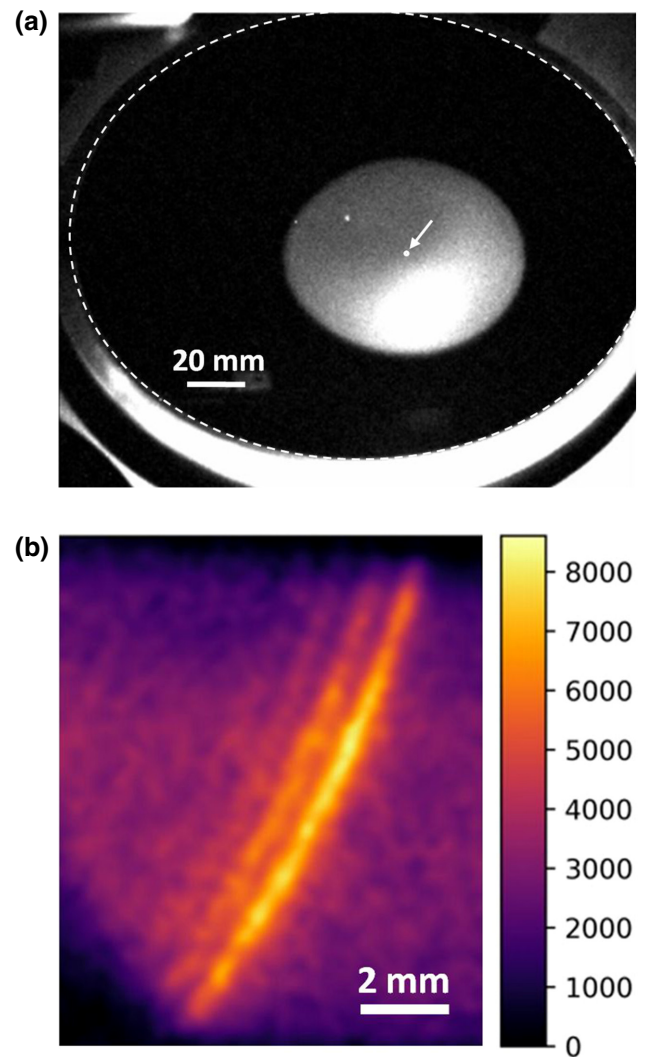


FIG. 2. Circular propagating crack front in ion-implanted crystalline silicon. (a) View with a high-speed camera. Silicon wafer (white dotted line) is bonded to a transparent thick oxide layer to allow live monitoring of the fracture. Exposure time is $0.5 \mu\text{s}$. White spot at the wafer center is the fractured area. Arrow indicates the location where the crack is initiated. (b) Synchrotron diffractive x-ray imaging on the Si 220 Bragg reflection in Laue geometry (ESRF-ID19). Illuminating x-ray pulse width is 55 ps and camera exposure time is $0.5 \mu\text{s}$. Brightest arc is the crack front; other trailing ones are due to previous x-ray pulses and afterglow of the scintillator used.

a constant-velocity moving Dirac delta emitter of acoustic waves, which travel over long distances with very low attenuation and experience normal reflection at substrate edges. A_0 and S_0 modes in silicon have group velocities up to 8 km/s and can thus propagate ahead of the crack. The A_0 mode is highly dispersive, allowing emergence by phase coherence of a single dominant acoustic frequency, the value of which is directly related to the crack velocity.

This fast-traveling signal interacts with the crack front after reflection from sample edges. By varying the local shear stress, the A_0 flexural Lamb mode modulates the crack-front trajectory between microcracks, causing periodic variations of the postfracture roughness. This modulation is detected under the form of regular fringe patterns with few-millimeter wavelengths on the surface. Since the crack is confined in a few-nanometer-thick plane and typical acoustic paths lengths (from mm to m) are large, relative to the plate thickness (~ 1.5 mm), both crack and wave propagations can be described as being two dimensional.

Here, we push these experiments one step further using large-sized full-wafer samples to delay and better separate direct and boundary-reflected wave effects on crack propagation. We show that, due to the self-interaction of different parts of the extended curved crack front through the fractured solid, regular complex patterns are formed. The proposed model assumes only flexural Lamb waves and yet can reproduce rather complex details, with no adjustable parameters.

The geometry used herein refers to the so-called strip geometry, where, as opposed to crack propagation in an infinitely thick sample, the crack velocity reaches an asymptotic value rapidly and remains constant. The large size and round geometry of defect-free wafers allow easier sampling and description of the produced acoustic waves, but are not expected to be system-specific.

II. FRACTURE PATTERNS ON LARGE ION-IMPLANTED SILICON SUBSTRATES

Experiments are performed with pairs of bonded 300 mm {100} crystalline silicon substrates. One substrate is thermally oxidized and implanted with light ions before hydrophilic bonding to the other. Following Smart-Cut technology flow, the assembly is then annealed. The fracture occurs along the implanted zone, achieving the transfer of a thin layer of monocrystalline silicon onto the handle substrate and creates a silicon-on-insulator structure. The crack velocity is measured *in situ* with lasers using the protocol described in Ref. [34]. Fractured surfaces are scanned to build roughness maps through the “haze” signal using light-scattering metrology (KLA-TENCOR Surfscan). This method records the intensity of light scattered by $5\text{--}80^\circ$ from a focused (~ 50 μm spot) 355 nm laser, thus so-called haze maps are constructed. The haze signal linearly depends on the square of the root-mean-square surface roughness in the $0.1\text{--}10$ μm^{-1} spatial frequency range.

Figure 3 presents typical postfracture haze maps of SOI wafers. Regular sets of fringes, named “fracture patterns,” are visible. Experimentally, three factors have a significant influence on their shape: the fracture initiation location, the crack velocity, and the wafer thickness. In the studied configuration, the fracture starts either from the wafer edge (“edge-initiated fracture”) or at a position inside

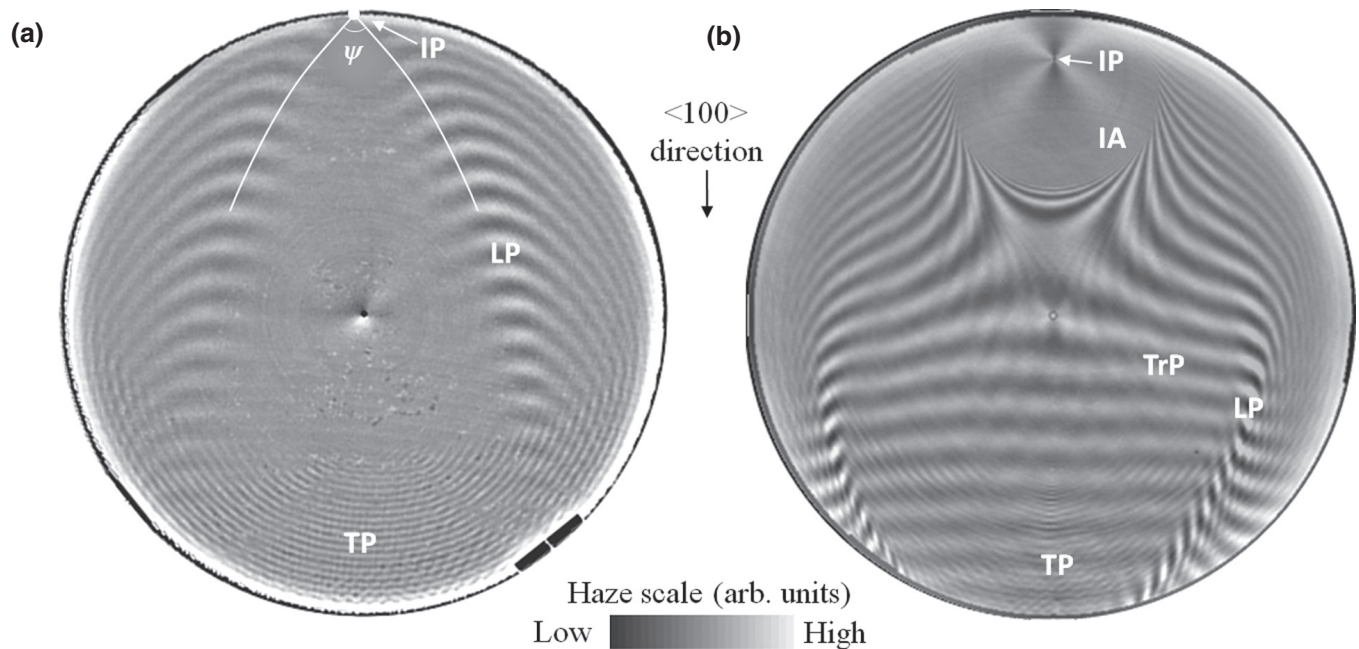


FIG. 3. Typical haze maps of SOI substrates after fracture. (a) Fracture pattern with fracture initiation at wafer edge ($v_f = 2500$ m/s). (b) Fracture pattern with fracture initiation in the wafer inner area ($v_f = 2400$ m/s). Letters give descriptions of fracture patterns: IP, initiation point; IA, initiation area; LP, lateral pattern; TP, terminal pattern; TrP, transverse patterns. Wafer diameter is 300 mm. Points at wafer center are light-scattering measurement artifacts.

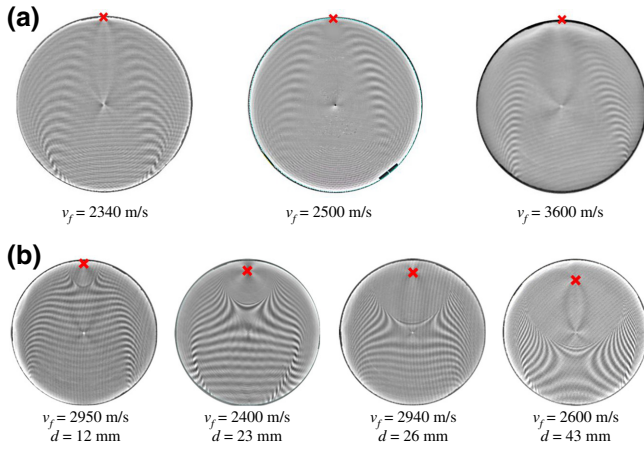


FIG. 4. (a) Edge-initiated fracture-pattern dependence on crack velocity v_f . (b) Inner wafer-initiated fracture pattern dependence on crack velocity and fracture-initiation distance to wafer edge, d . Fracture-initiation positions are marked with crosses. Silicon wafer diameter is 300 mm. Point and cross patterns at wafer center are light-scattering measurement artifacts. Regular curved lines are traces of implantation beam scanning, which is unrelated to the fracture pattern.

the bonded pair (“inner wafer-initiated fracture”). Fracture patterns are always aligned with respect to the average crack-propagation direction defined by the vector between the initiation point and the wafer center.

For edge-initiated fracture, the pattern is made of two lateral curved bands crossing the wafer with centimeter-wavelength (lateral pattern) and semicircular millimeter-sized fringes parallel to the wafer edge and located at the end of the fracture propagation (terminal pattern) [Fig. 3(a)]. Inner wafer-initiated patterns are more complex with additional fringes, the wavelength of which is similar to that of the lateral pattern (transverse pattern) and a zone without haze variation around the fracture initiation position (initiation area) [Fig. 3(b)].

The dimension δ of the initiation area is found to be proportional to the distance d between the initiation point and the sample edge. Typical pattern lengths (fringe wavelengths and initiation area size) decrease when the wafer thickness is reduced or if the crack velocity is increased (Fig. 4). Beyond these three factors, fracture-pattern reproducibility between wafers is remarkable, indicating very low dependence on other parameters.

III. INTERACTION MODEL BETWEEN CRACK FRONT AND LAMB WAVES

To investigate the shape of fracture patterns in circular geometry, we assume that their origin lies in the interactions of the crack front with self-emitted A_0 Lamb modes, as reported earlier [34]. In this case, local haze modulations at the wafer surface happen when the crack front “prints” on the fractured surface the local amplitude of shear stress

as it passes. The postfracture haze signal is assumed, for a given position M , to be directly related to the amplitude of the A_0 Lamb mode at M when the crack reaches this point.

For low frequencies, antisymmetric A_0 Lamb waves are flexural modes of thin plates. Considering the silicon substrates as isotropic plates, with thickness h , density ρ , Young’s modulus E , and Poisson’s ratio ν , the local vertical displacement ζ at time t and distance r from a point excitation force f must follow the propagation equation [38]:

$$\left(D\nabla^4 + \rho h \frac{\partial^2}{\partial t^2}\right) \zeta(r, t) = f(r, t) \text{ with } D = \frac{E h^3}{12(1 - \nu^2)} \quad (1)$$

A solution of Eq. (1) can be built from the Green function for an infinite plate $G_\infty(r, t)$ in terms of Bessel functions and harmonic waves of angular frequency ω [39]. The wave number k is then given by

$$k = \left(\omega^2 \frac{\rho h}{D}\right)^{1/4}. \quad (2)$$

For $kr \gg 1$, the solution can be simply written using Bessel’s function asymptotic expansions

$$\zeta(r, t) = G_\infty(r, t) \approx \sqrt{\frac{2}{\pi}} \frac{e^{-i\pi/4}}{8Dk^2} \frac{e^{i(kr - \omega t)}}{\sqrt{kr}}. \quad (3)$$

Phase and group velocities v_ϕ and v_g are related by a factor of two. C_P is thus a fraction of the longitudinal wave velocity:

$$v_\phi = \frac{\omega}{k} = C_P k h \quad v_g = \frac{\partial \omega}{\partial k} = 2C_P k h \text{ with} \\ C_P = \sqrt{\frac{E}{12\rho(1 - \nu^2)}}. \quad (4)$$

Throughout propagation across the wafers, every part of the crack front is considered as a Lamb wave point “white” emitter (a Dirac in time space) and interference occurs everywhere. Visible patterns are obtained when constructive interference happens and produces large roughness amplitudes on surfaces.

Considering the self-interaction of a crack with its own acoustic emission, a constant crack velocity, v_f , and a circular front shape, a signal emitted from position S at time t_s will contribute to the Lamb amplitude when the crack passes through M at time t_M only if its group velocity satisfies the following equation:

$$l = v_g(\omega, k)(t_M - t_s) \quad (5)$$

where l is the length of the acoustic path between S and M , $t_M = R/v_f$, and $t_s = r/v_f$ (Fig. 5). According to the A_0

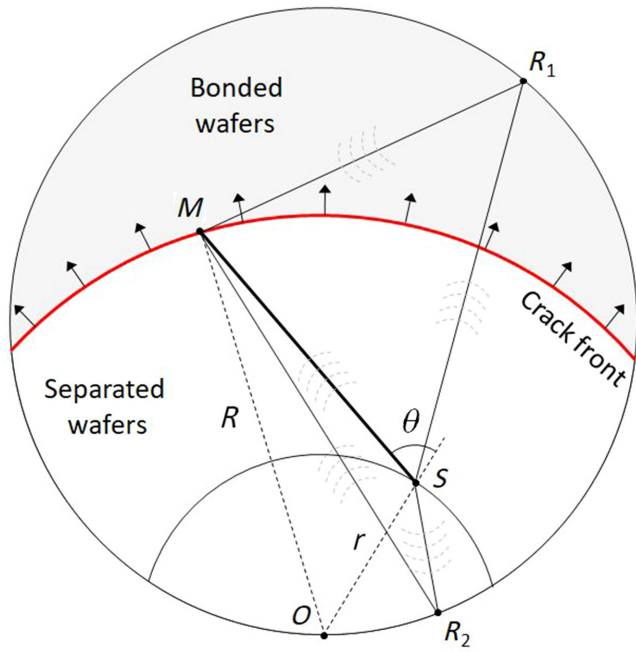


FIG. 5. Acoustic paths between source S and point M . Direct path ($S \rightarrow M$) and reflected path ($S \rightarrow R_2 \rightarrow M$) in separated wafers, and reflected path in bonded wafers ($S \rightarrow R_1 \rightarrow M$). Acoustic signals under consideration are emitted when the crack passes through S and influence the crack when they reach M . Crack front starts at position O and retains constant velocity and circular shape.

dispersion relation in silicon, there is no solution if v_g exceeds the maximum velocity of A_0 Lamb modes ($v_g^{\max} = 4637$ m/s for silicon $\langle 100 \rangle$; see Appendix). Except for high values, where two solutions exist ($v_g > 4375$ m/s in silicon $\langle 100 \rangle$), a unique frequency satisfies Eq. (5). Because the Lamb dispersion relation depends on the plate thickness, this frequency will not be the same in the separated wafers (waves propagating behind the crack) and the bonded substrates (waves propagating in front of the crack).

Unlike in the pseudo-1D case [34], the size and shape of the system make several acoustic paths possible between a given pair of points (S, M) [Fig. 5]. As the crack front is curved, a signal can go from S to M without reflection on wafer edges by propagating in the separated wafers just behind the crack front (direct path). Their radial velocity is then close to the crack velocity, so that, in a frame linked to the crack, they move essentially along the crack.

Reflected paths also exist because Lamb modes can travel long distances with very low losses [40,41]. For the low frequencies, their reflection on edges can be considered as normal without mode conversion [42–44]. Two or four paths with a single normal reflection between S and M are geometrically possible and can contribute to the acoustic signal at the crack front. When the reflection point is in

front of (behind) the crack, propagation usually happens in bonded (separated) wafers. Some reflective paths tangential to the crack front can cross it during their propagation, but their contribution is negligible and will not be taken into account. If multiple reflection paths are geometrically possible, they would mainly require very fast propagating waves, not available as A_0 modes. Because they are highly unlikely, they will also not be considered in this work.

Figure 5 illustrates the three types of acoustic paths possible between a source S and a point M on the crack front: direct path in separated wafers ($S \rightarrow M$), reflected paths in bonded wafers ($S \rightarrow R_1 \rightarrow M$), and reflected paths in separated wafers ($S \rightarrow R_2 \rightarrow M$).

Combining Eqs. (4) and (5) and considering all waves L_j satisfying Eq. (5) and all acoustic paths P_i , the contribution $\zeta(S, M)$ of a source S to the signal at position M can be written as

$$\zeta(S, M) = \sum_{P_i} \sum_{L_j} \frac{a}{k^2_{i,j} \sqrt{k_{i,j} l_{i,j}}} e^{-i \cdot \phi_{i,j}(S, M)} \quad \text{with} \quad (6)$$

$$\phi(S, M) = kl \left(1 - \frac{v_\phi}{v_g} \right).$$

The radiated acoustic power is assumed to be constant over time. The amplitude $Z(M)$ of the A_0 Lamb mode at position M is the sum of all contributions from all sources located on the crack front at any time before it reaches M . Considering that all points of the crack front radiate in the same way, everywhere and anytime,

$$Z(M) = \int \int_{S(t_s < t_M)} \zeta(S, M) dS. \quad (7)$$

Using this model, fracture patterns are calculated by numerically computing the sum of Eq. (7) for each position M of the wafer. Silicon A_0 dispersion models for propagation in directions $\langle 100 \rangle$ and $\langle 110 \rangle$ are used to cover the whole range of possible frequencies [45] (see Appendix). For each combination (S, M), direct and reflective acoustic paths are geometrically built, and Eq. (5) is solved.

IV. MODEL VALIDATION

To evaluate the ability of the model to predict fracture patterns, a set of wafers with different crack velocities and initiation locations are selected. For each substrate, the experimental haze map is compared to the pattern calculated using the model previously described, and the crack velocity is experimentally measured. For edge-initiated fracture [Fig. 6(a)] and for inner wafer-initiated fracture [Fig. 6(b)], there are excellent agreements between experimental and calculated patterns, both regarding the overall pattern shape and their dependence on crack velocity and initiation location. The variation of the fringe period with

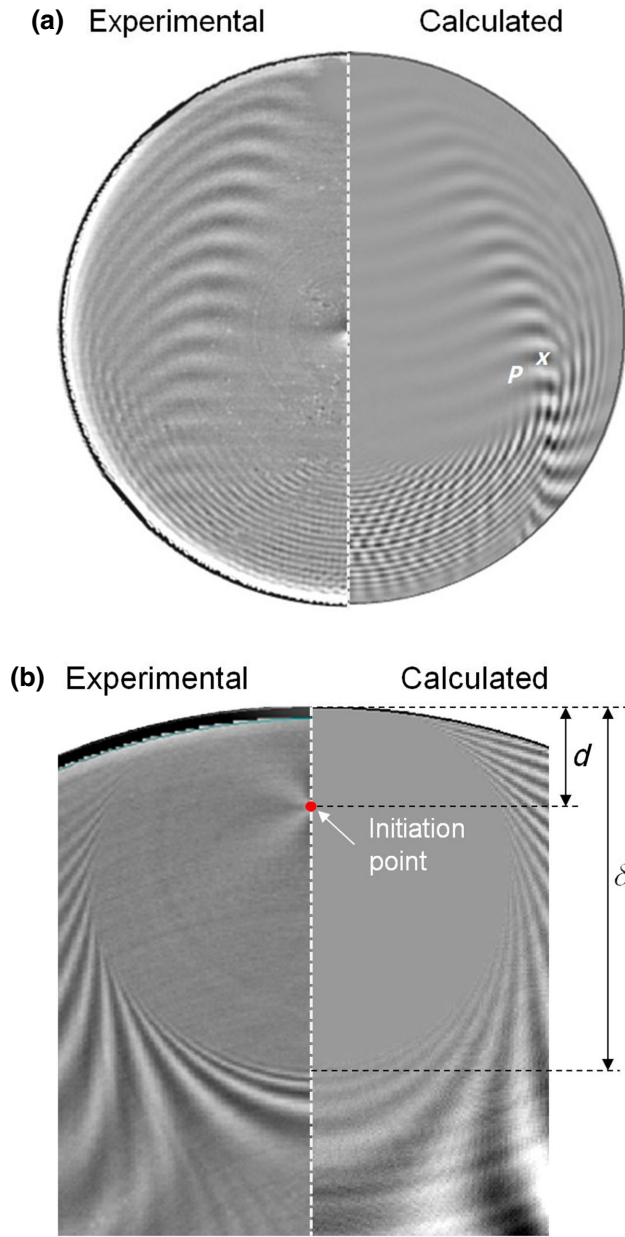


FIG. 6. Comparison of experimental fracture pattern (left) with model calculation (right). (a) Edge-initiated fracture ($v_f = 2500$ m/s). (b) Detail around the initiation area for inner wafer-initiated fracture ($v_f = 2400$ m/s).

crack velocity is also well predicted, with experimental wavelengths between the calculated values for $\langle 100 \rangle$ and $\langle 110 \rangle$ directions [Fig. 7(a)].

The model allows the determination of which acoustic path makes a dominant contribution to the different parts of patterns. The lateral fringes are made by the direct acoustic paths traveling behind the crack in the separated wafers. For low-frequency waves, where $v_g \approx 2v_\phi$, the phase shift between S and M , $\phi(S, M)$, can be written by combining Eqs. (5) and (6), so that it depends only on elastic

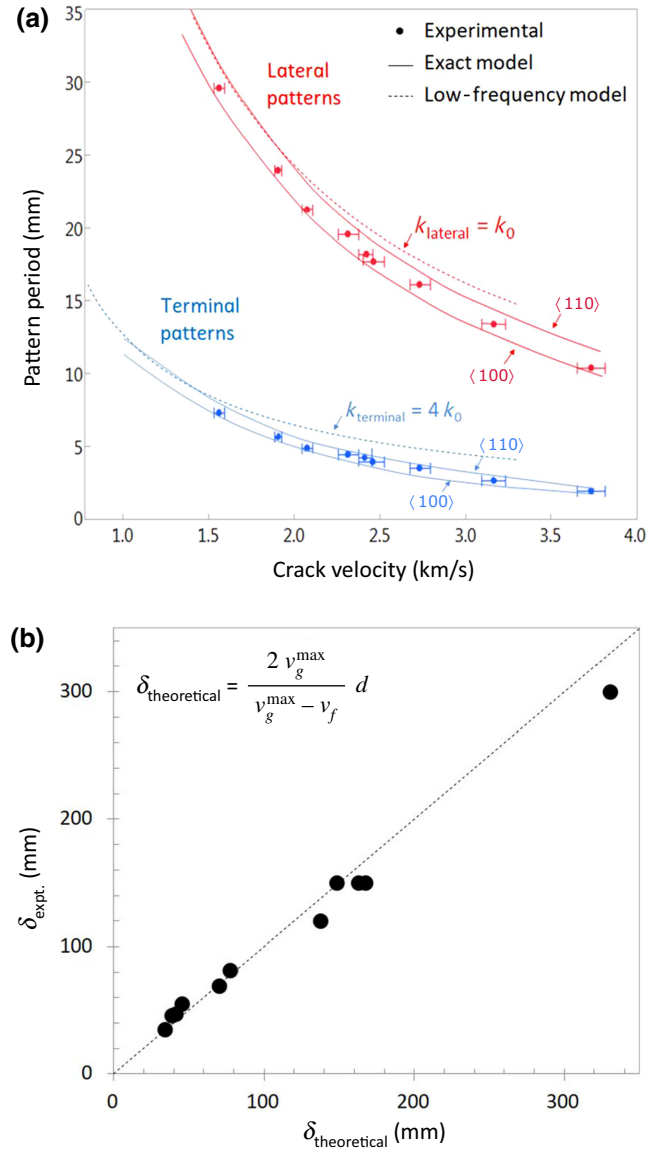


FIG. 7. (a) Experimental and calculated evolution of fracture-pattern fringe periods with crack velocity. (b) Comparison of experimental and predicted extension of initiation area (δ).

parameters and geometry:

$$\phi(S, M) = \frac{kl}{2} = k_0 \frac{l^2}{(R-r)} \quad \text{with} \quad k_0 = \frac{v_f}{4C_p h}. \quad (8)$$

For direct paths and low θ angle, l is very close to $R-r$ [Fig. 5]. This makes it possible to approximate Eq. (7) by $Z(M) = A + B \exp(-ik_0 R)$, with A and B constant. The lateral-pattern wavelength is then close to $2\pi/k_0$, which is in excellent agreement with experimental data, when low-frequency waves are dominant in pattern creation, i.e., for low crack velocities [Fig. 6(a)].

The reflected path in separated wafers causes the transverse pattern and initiation area. Using Eq. (8), the

transverse-pattern typical wavelength is found to be identical to those of lateral patterns, in good agreement with experiments.

For inner wafer-initiated fractures, no reflective path in separated wafers exists until the crack front reaches the substrate edge. The pattern-free initiation area corresponds to the time interval during which the crack progresses in the absence of any reflected A_0 mode. The extension δ of the initiation area can then be written simply as

$$\delta = \frac{2v_g^{\max}}{v_g^{\max} - v_f} d. \quad (9)$$

For a given crack velocity, δ is proportional to d , which is the distance between the fracture-initiation point and the edge of the substrate [Fig. 6(b)], in good agreement with experiments [Fig. 7(b)].

Finally, reflected paths in bonded wafers create the terminal pattern in the same way as that for linear samples [34]. Because propagation occurs in a plate of thickness $2h$, the associated fringes have a wave number of $k_{\text{terminal}} = v_f / (C_p h) = 4k_0$, in line with experimental values [Fig. 7(a)].

V. DISCUSSION

The geometrical calculation of the crack-front interaction with its self-emitted acoustic waves predicts well the geometries observed on circular plates. The model highlights that each family of acoustic paths creates specific features of the overall pattern. The crack front interacts simultaneously with three different kinds of acoustic signals: a single-frequency mode reflected into the bonded wafers; a wave train propagating just behind the crack front; and a signal reflected into the fractured area, propagating over long distances. The complexity of the experimental patterns stems from the overlap of all of these contributions.

Considering the model assumptions, patterns finally depend only on a few macroscopic parameters: crack characteristics (velocity, initiation position, and front shape), silicon elastic parameters (through the dispersion curves of the A_0 Lamb mode), and the system's geometry (substrate shape and thickness). As silicon wafers for electronic applications have extremely tight specifications, in terms of material and dimensions, fracture patterns are very repeatable from wafer to wafer.

While the signal emitted in front of the fracture is acting only for terminal patterns, lateral and transverse patterns imply waves propagating behind the crack front, in separated wafers. The acoustic signal first has to move away and then catch up with the crack. With the reflected path, it is obviously possible when the signal is returned toward the crack after reflection on system edges. For transverse patterns, the fastest Lamb waves move away from the

crack over distances of up to about the substrate radius before coming back. In contrast, the acoustic signal of lateral patterns follows the direct path and spreads at an average distance of five wavelengths strictly behind and independently from the crack front, the shape of which is not modified. As an example, at point P in Fig. 6(a), the model indicates that 50% of the A_0 waves involved in direct interactions never deviate more than 2.5 mm from the crack during their propagation, even if the overall average path length is 136 mm. Thus, in the crack-front reference frame, this acoustic emission is like a wave train slowly propagating just behind the crack front before interacting again. This situation is, however, different from the crack-front waves that are essentially nondispersive, propagate on the crack front at the Rayleigh wave velocity, and originate in asperities that change the material fracture toughness locally, and hence, the crack-front velocity. Their typical period relates to the size of the perturbation and can be very different from the wavelength of the acoustic patterns.

A wide range of A_0 Lamb waves, with wavelengths from tenths of a millimeter to centimeters, equally contribute to the formation of the different fracture patterns. In front of the crack, a dominant monofrequency A_0 mode ($v_\phi = v_f$) emerges because of the stationary-phase principle and defines the terminal pattern geometry [34]. The waves involved in the lateral pattern (related to direct paths) have only their radial velocities in common, close to v_f , and are responsible for the observed fringe period ($2\pi/k_0$). This typical length emerges when the crack makes a localized nondisturbing sampling of the Lamb's amplitude and is not related to any preselected frequency of the acoustic spectrum traveling in the fractured parts [34].

The intensity of lateral patterns is difficult to fully predict analytically. The position of the two symmetrical bands of fringes corresponds to locations where isophase lines [$\varphi(S, M) = \text{constant}$] are parallel to the substrate edges, meaning that a small shift in position causes a large variation of the total amplitude $Z(M)$ and leads to well-contrasted fringes. Since these patterns do not involve reflected paths, system edges determine only the band positions because they impose a limited size to the crack front. With a half-plane plate shape (i.e., a wafer with infinite radius), the crack front is a semicircle of increasing radius and edge-initiated lateral patterns turn to simple V shapes with invariant angle ψ close to 80° [Fig. 3(a)]. In an infinite plane with no boundaries, which is the case at the early times of inner wafer-initiated fracture, the crack front is a full circle, and therefore, does not produce bands of fringes.

Fracture patterns are experimentally observed with other materials, where guided fracture can be made by ion implantation. This includes a wide range of brittle materials, in which the diffusion of light-implanted species is low, like semiconductors (Ge, AsGa, InP, GaN, SiC) or oxides

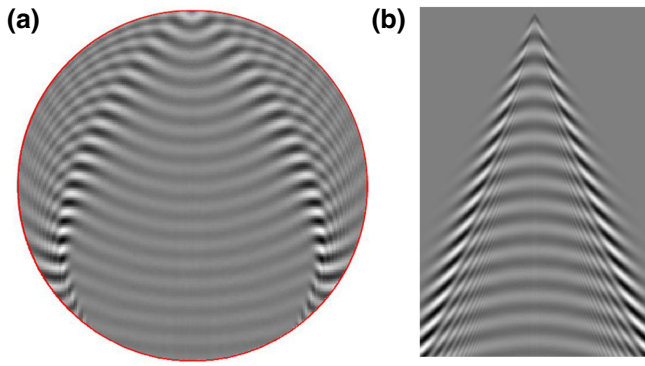


FIG. 8. Examples of geometrical patterns created by the movement of a finite-size moving source into a dispersive medium. (a) Calculated fracture pattern in silicon (direct acoustic paths only, edge-initiated fracture, $v_f = 2500$ m/s, enhanced contrast, fracture start at top). (b) Calculated Kelvin wake pattern (Froude number $Fr = 2.25$, moving source at top).

(sapphire, LiTaO_3 , LiNbO_3) [46]. However, the observation of regular and well-defined fracture patterns, such as those of silicon, is not common. A favorable ratio between fracture and acoustic wave velocities is needed, so that the fringe dimensions are small enough, in relation to the sample size, and are observable. A sufficient coupling between crack and acoustic waves is also mandatory to produce detectable roughness variations on postfracture surfaces.

Such emergence of localized constructive interference created by the impulse response of a moving source with finite size into a dispersive medium evokes Kelvin wake patterns, where a point source travels on a liquid surface exciting gravity waves [47]. Even if there is not a complete analogy, with extended versus point sources, a certain similarity exists between the two types of shapes (Fig. 8) that share common characteristics, such as the main wake angle, which is independent of the object's velocity.

VI. CONCLUSION

The study of postfracture surface patterns in ion-implanted silicon plates shows that, fundamentally, a crack front can interact with its own acoustic emission via elastic waves propagating behind it with no frequency preselection or modification of crack dynamics. Furthermore, the interaction is possible without reflection at system edges if the crack front is curved. As with ship wakes, this research highlights the rise of complex regular structures from the displacement of a finite object (a crack front) in a dispersive medium (thin silicon plates) through self-produced elastic waves (Lamb waves).

ACKNOWLEDGMENTS

This work is supported by the project FRAINDY of the French National Research Agency (ANR).

The authors declare no competing financial interests.

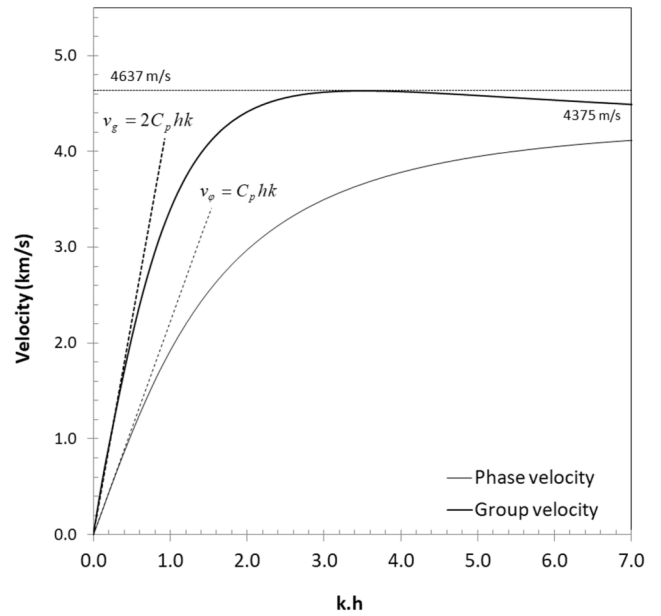


FIG. 9. A_0 Lamb mode dispersion diagram of silicon in the $\langle 100 \rangle$ direction, as used in the fracture-pattern model. Group velocity v_g , and phase velocity v_ϕ , are plotted versus wave number, k , and plate thickness, h .

APPENDIX: A_0 LAMB MODE DISPERSION DIAGRAM OF SILICON

Theoretical solutions for the Lamb dispersion curves are computed using the Waveform revealer software [45] and the mechanical elastic properties of silicon wafer material. Figure 9 shows the calculated dispersion diagram for silicon $\langle 100 \rangle$ used in the model for fracture pattern calculations.

- [1] E. David, R. Schall, and H. Schardin, in *Stress Waves in Anelastic Solids*, edited by H. Kolsky and W. Prager, (Springer-Verlag, Berlin, 1964), p. 187.
- [2] H. G. Richter and F. Kerkhof, in *Fractography of Glass*, edited by R.C. Bradt and R.E. Tressler, (Plenum Press, New York, 1994), pp. 75–109.
- [3] S. Yoshida, J. Matsuoka, and N. Soga, Evaluation of crack growth in glass by using stress-wave fractography, *J. Am. Ceram. Soc.* **82**, 1621 (1999).
- [4] D. Bonamy and K. Ravi-Chandar, Interaction of Shear Waves and Propagating Cracks, *Phys. Rev. Lett.* **91**, 235502 (2003).
- [5] J. F. Boudet, S. Ciliberto, and V. Steinberg, Experimental study of the instability of crack propagation in brittle materials, *Europhys. Lett.* **30**, 337 (1995).
- [6] J. Shen, W. Z. Liang, and J. F. Su, Formation of nanowaves in compressive fracture of a less-brittle bulk metallic glass, *Appl. Phys. Lett.* **89**, 121908 (2006).
- [7] H. Wallner, Linienstrukturen an bruchflächen, *Zeitschrift für Physik* **114**, 368 (1939).

- [8] E. H. Andrews, Stress Waves, and Fracture Surfaces. *J. Appl. Phys.* **30**, 740 (1959).
- [9] D. Hull, *Fractography: Observing, Measuring and Interpreting Fracture Surface Topography* (Cambridge University Press, Cambridge, England, 1999).
- [10] A. Rabinovitch, Wallner lines revisited, *J. Appl. Phys.* **99**, 076102 (2006).
- [11] K. Ravi-Chandar and W. G. Knauss, On the interaction of stress waves with propagating cracks, *Int. J. Fract.* **26**, 189 (1984).
- [12] J. F. Boudet and S. Ciliberto, Interaction of Sound with Fast Crack Propagation, *Phys. Rev. Lett.* **80**, 341 (1998).
- [13] A. M. Fitzgerald, T. W. Kenny, and R. H. Dauskardt, Stress wave interference effects during fracture of silicon micromachined specimens, *Exp. Mech.* **43**, 317 (2003).
- [14] L. M. Wang, L. Zhao, M. Fourmeau, and D. Nelias, Crack plane deflection and shear wave effects in the dynamic fracture of silicon single crystal, *J. Mech. Phys. Solids* **122**, 472 (2019).
- [15] M. Marder, New Dynamical Equation for Cracks, *Phys. Rev. Lett.* **66**, 2484 (1991).
- [16] T. Goldman, A. Livne, and J. Fineberg, Acquisition of Inertia by a Moving Crack, *Phys. Rev. Lett.* **104**, 114301 (2010).
- [17] J. Morrissey and J. Rice, Perturbative simulations of crack front waves, *J. Mech. Phys. Solids* **48**, 1229 (2000).
- [18] E. Bouchaud, J. P. Fisher, D. S. Ramanathan, and J. R. Rice, Can crack front waves explain the roughness of cracks?, *J. Mech. Phys. Solids* **50**, 1703 (2002).
- [19] E. Sharon, G. Cohen, and J. Fineberg, Propagating solitary waves along a rapidly moving crack front, *Nature* **410**, 68 (2001).
- [20] J. Fineberg, E. Sharon, and G. Cohen, Crack front waves in dynamic fracture, *Int. J. Frac.* **119**, 247 (2003).
- [21] L. Zhao, D. Bardel, A. Maynadier, and D. Nelias, Velocity correlated crack front and surface marks in single crystalline silicon, *Nat. Commun.* **9**, 1298 (2018).
- [22] S. P. Gross, J. Fineberg, M. Marder, W. D. McCormick, and H. L. Swinney, Acoustic Emissions From Rapidly Moving Cracks, *Phys. Rev. Lett.* **71**, 3162 (1993).
- [23] A. G. Evans and M. Linzer, Failure prediction in structural ceramics using acoustic emission, *J. Am. Ceram. Soc.* **56**, 11 (1973).
- [24] S. Cousland and C. Scala, Acoustic emission during the plastic deformation of aluminium alloys 2024 and 2124, *Mater. Sci. Eng.* **57**, 23 (1983).
- [25] S. Bouras, I. Zerizer, F. Gheldane, M. T. Bouazza, and B. Bouzabata, Study of the resistance to crack propagation in alumina by acoustic emission, *Ceram. Int.* **34**, 1857 (2008).
- [26] J. L. Rose, Ultrasonic guided waves in structural health monitoring, *Key Eng. Mater.* **270-273**, 14 (2004).
- [27] K. Holford, M. J. Eaton, J. J. Hensman, R. Pullin, S. L. Evans, N. Dervilis, and K. Worden, A new methodology for automating acoustic emission detection of metallic fatigue fractures in highly demanding aerospace environments: An overview, *Prog. Aerosp. Sci.* **90**, 1 (2017).
- [28] H. Moriceau, F. Rieutord, F. Fournel, Y. Le Tiec, L. Di Cioccio, C. Morales, A. M. Charvet, and C. Deguet, Overview of recent direct wafer bonding advances and applications, *Adv. Nat. Sci. Nanosci. Nanotechnol.* **1**, 043004 (2010).
- [29] J. D. Penot, D. Massy, F. Rieutord, F. Mazen, S. Reboh, F. Madeira, L. Capello, D. Landru, and O. Kononchuk, Development of microcracks in hydrogen-implanted silicon substrates, *J. Appl. Phys.* **114**, 123513 (2013).
- [30] M. Bruel, Silicon on insulator material technology, *Electron. Lett.* **31**, 1201 (1995).
- [31] B. Aspar, M. Bruel, H. Moriceau, C. Maleville, T. Poumeyrol, A. M. Papon, A. Claverie, G. Benassayag, A. J. Auberton-Hervé, and T. Barge, Basic mechanisms involved in the smart-Cut process, *Microelectron. Eng.* **36**, 233 (1997).
- [32] S. Reboh, F. Rieutord, L. Vignoud, F. Mazen, N. Cherkashin, M. Zussy, D. Landru, and C. Deguet, Effect of H-implantation in the local elastic properties of silicon crystals, *Appl. Phys. Lett.* **103**, 181911 (2013).
- [33] D. Massy, F. Mazen, S. Tardif, J. D. Penot, J. Ragani, F. Madeira, D. Landru, O. Kononchuk, and F. Rieutord, Fracture dynamics in implanted silicon, *Appl. Phys. Lett.* **107**, 092102 (2015).
- [34] D. Massy, F. Mazen, D. Landru, N. Ben Mohamed, S. Tardif, A. Reinhardt, F. Madeira, O. Kononchuk, and F. Rieutord, Crack Front Interaction with Self-Emitted Acoustic Waves, *Phys. Rev. Lett.* **121**, 195501 (2018).
- [35] H. Lamb, On waves in an elastic plate, *Proc. R. Soc. London Math. Phys. Eng. Sci.* **93**, 114 (1917).
- [36] V. Giurgiutiu, Tuned lamb wave excitation and detection with piezoelectric wafer active sensors for structural health monitoring, *J. Intell. Mater. Syst. Struct.* **16**, 291 (2005).
- [37] T. Sato, M. Takemoto, and K. Ono, Effect of fracture dynamics in thin plate on the waveform and radiation pattern of the lamb waves, *Jpn. J. Appl. Phys.* **38**, 3193 (1999).
- [38] K. J. Graff, *Wave Motion in Elastic Solids* (Dover, New York, 1991).
- [39] E. G. Williams, *Fourier Acoustics: Sound Radiation and Nearfield Acoustic Holography* (Academic Press, London, 1999).
- [40] M. D. Seale, B. T. Smith, and W. H. Prosser, Lamb wave assessment of fatigue and thermal damage in composites, *J. Acoust. Soc. Am.* **103**, 2416 (1998).
- [41] J. L. Rose, A baseline and vision of ultrasonic guided wave inspection potential, *J. Pressure Vessel Technol.* **124**, 273 (2002).
- [42] A. Gunawan and S. Hirose, Reflection of obliquely incident guided waves by an edge of a plate, *Mater. Tran.* **48**, 1236 (2007).
- [43] Z. Ahmad and U. Gabbert, Simulation of lamb wave reflections at plate edges using the semi-analytical finite element method, *Ultrasonics* **52**, 815 (2012).
- [44] S. Santhanam and R. Demirli, Reflection of lamb waves obliquely incident on the free edge of a plate, *Ultrasonics* **53**, 271 (2013).
- [45] V. Giurgiutiu, *Waveform Revealer* (University of South Carolina, Laboratory for active materials and smart structures (LAMSS), Columbia, 2013).
- [46] B. Aspar, H. Moriceau, E. Jalaguier, C. Lagahe, A. Soubie, B. Biasse, A. M. Papon, A. Claverie, J. Grisolia, G. Benassayag, et al., The generic nature of the smart-Cut process for thin film transfer, *J. Electron. Mater.* **30**, 834 (2001).
- [47] L. Kelvin, On the waves produced by a single impulse in water of any depth, or in a dispersive medium, *Proc. R. Soc. London, Ser. A* **42**, 80 (1887).